Three-dimensional preparation and imaging reveal intrinsic microtubule properties

Philipp J Keller, Francesco Pampaloni & Ernst H K Stelzer

We present an experimental investigation of microtubule dynamic instability in three dimensions, based on laser light-sheet fluorescence microscopy. We introduce three-dimensional (3D) preparation of *Xenopus laevis* egg extracts in Teflon-based cylinders and provide algorithms for 3D image processing. Our approach gives experimental access to the intrinsic dynamic properties of microtubules and to microtubule population statistics in single asters. We obtain evidence for a stochastic nature of microtubule pausing.

Microtubules, which are cytoskeletal filaments found in all eukaryotes, have a fundamental role in cell division, intracellular trafficking, cell motility as well as in development and maintenance of cell shape[1]. They are highly dynamic structures that stochastically undergo phases of growth and shrinkage (dynamic instability)[2].

Until now, microtubule dynamic instability has been investigated in two-dimensional (2D) preparations, mainly by epifluorescence[3], video-enhanced differential interference contrast[4], confocal[5] and dark-field microscopies[6]. In a conventional experimental arrangement samples are prepared in shallow, quasi 2D chambers, delimited by flat and hard glass surfaces[5]. Although 2D assays are well-established and straightforward in their application, a 3D approach to studies of microtubule dynamic instability is desirable for several reasons. Previous studies have provided evidence for a considerable influence of microtubule-surface interactions on microtubule dynamic instability[7,8] as well as for an alteration of diffusion processes resulting from the choice of a specific compartment volume[9]. Therefore, biases introduced by the mechanical constraints and the proximity of the hard glass surfaces to the dynamic microtubules cannot be ruled out in 2D assays. More importantly, some experimental aspects of microtubule behavior can only be determined in a truly 3D system.

We present a method for 3D analysis of microtubule dynamic instability. We used single plane illumination microscopy (SPIM), one of EMBL's implementations of laser light sheet–based fluorescence microscopy, for the purpose of 3D time-resolved imaging[10,11] (see **Supplementary Methods** and **Supplementary Video 1** online). SPIM allows the continuous recording of microtubule aster dynamics in three dimensions with minimal photoinduced damage[11] and good spatiotemporal resolution (**Supplementary Videos 2** and **3** online). For 3D sample preparation, we transferred interphase *X. laevis* egg extracts to cylindrical chambers with 25-μm thin transparent Teflon-based walls and a diameter of 2 mm (**Supplementary Fig. 1** online), thereby reducing the surface-to-volume ratio by a factor of 50 compared to the preparation between two closely spaced (10–20 μm) glass plates[11]. This system facilitates the observation of microtubule dynamics under minimally constrained 3D conditions (**Fig. 1**) and allows distinguishing between intrinsic events of dynamic instability and events triggered by microtubule-surface contact. We developed both user-guided and automated image processing algorithms to analyze the filament's 3D geometry and the dynamics in three dimensions over time (**Supplementary Methods**, **Supplementary Software**, **Supplementary Figs. 2–4** and **Supplementary Video 4** online).
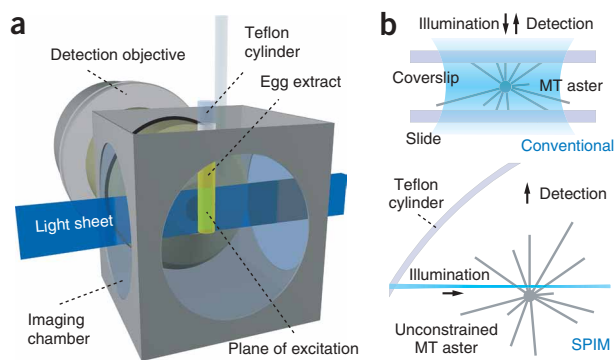

Figure 1 | Measurement of 3D microtubule dynamic instability. (**a**) Illustration (to scale) of the light sheet–based imaging arrangement at the sample chamber. The focal plane of the objective lens is co-planar with the light sheet. (**b**) Conventional 2D (top) and new 3D (bottom) experimental layouts. The 2D approach uses wide-field microscopy and sample preparation in a thin volume between slide and cover slip. Since the entire specimen is illuminated, conventional image acquisition of a single plane results in photodamage to the entire aster. The glass coverslip and slide introduce closely spaced surfaces and provide a physical obstacle to microtubule growth. In contrast, the 3D approach uses 3D imaging (SPIM) in combination with 3D sample preparation. The distance between the cylinder's surface and the recorded aster is in the order of 100 μm. The 3D data are recorded by moving the sample cylinder through the light sheet, ensuring that only the in-focus plane of the microtubule aster is illuminated.
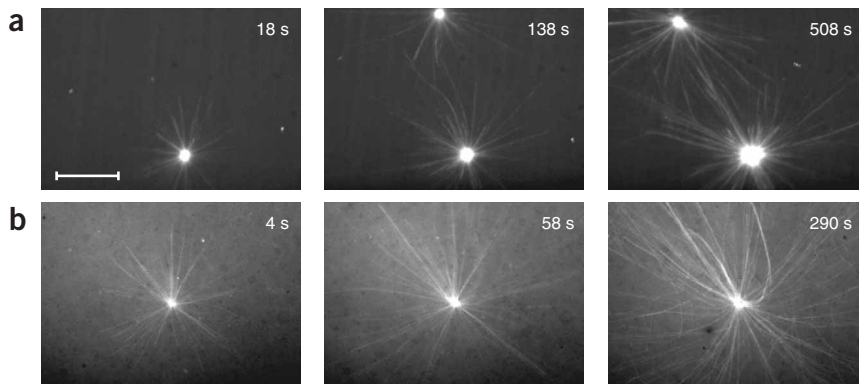
Figure 2 | Side-by-side comparison of 2D and 3D experiments of microtubule dynamic instability. (**a**) Maximum-intensity projections of a SPIM time-lapse 3D recording in interphase *X. laevis* egg extract. Each projection is based on 28 planes recorded at a spacing of 700 nm. Tubulin was labeled at a low ratio with Alexa-488. Elapsed time is relative to the start time of imaging. For all experiments, imaging started 1–2 min after the onset of microtubule polymerization. A global time axis can be reconstructed by population statistics (**Fig. 4a**). Carl Zeiss Achroplan 100×, 1.0 NA water objective. (**b**) Widefield fluorescence images (recorded with a Carl Zeiss Axiovert 135 TV microscope) using the conventional 2D assay (cover slip and slide sample preparation). Many microtubules are only partially or not at all located within the focal plane. A low labeling ratio of Alexa-488–tubulin produced images with a very low contrast and did not yield analyzable data. To obtain these images, a high labeling ratio Cy3-tubulin was used. Carl Zeiss Plan-Apochromat 100×, 1.4 NA oil objective. Scale bar, 10 μm.

To evaluate the influence of mechanical constraints of the experimental system on the microtubules' dynamic behavior, we performed a side-by-side comparison of microtubule dynamic instability in our 3D and in conventional 2D experimental configurations. We used identical protocols for *X. laevis* egg extract preparation, identical temperatures during the recordings (20 °C) and identical biochemical sample preparations (except for tubulin markers; **Figs. 1** and **2** and **Supplementary Methods**). We analyzed the kinetics of 18 microtubule asters in total ($n = 156$) in 12 independently prepared interphase egg extracts using both 2D and 3D experimental systems and identical image-processing and data-analysis routines.

The results of the 2D measurements were in very good agreement with previous 2D studies of interphase microtubule dynamic instability in *X. laevis* egg extracts, in particular with those that used different tubulin markers[3] (**Supplementary Table 1** online). The comparison of 2D and 3D state contributions to microtubule dynamic instability indicates that shrinkage events are, by a factor of 12, more frequent in the 2D system (**Table 1**). Although growth speeds differ by a factor of 2, shrinkage speeds agree well. This could be explained by the fact that microtubule polymerization speeds, in contrast to depolymerization speeds, are influenced by the diffusion of tubulin, which differs in 2D and 3D compartments[9]. As the experimental conditions in both systems are identical except for the surface-to-volume ratios, the observed differences in microtubule

shrinkage probability can be attributed to the external physical constraints. When comparing the images, additional differences between the two approaches become apparent. Within 2–3 min after the onset of microtubule polymerization, the mechanical stress introduced by two closely spaced glass surfaces in the 2D system affects the aster's geometry (**Fig. 2b**). Many microtubules are bent or exhibit local buckling. The plus-end tips of microtubules contact neighboring filaments, often triggering shrinkage. Eventually, some of the longer microtubules detach from the centrosome and move across the field of view by motor activity on the glass surfaces. We did not observe detaching or local buckling of microtubules in the 3D system. Thermal fluctuations, however, also lead to microtubule bending in three dimensions (**Fig. 2a**). These intrinsic fluctuations in filament shape allow us to determine elastic properties of microtubules in three dimensions.

Previous studies provide strong evidence for an alteration of microtubule dynamic instability through microtubule-surface interactions[7,8], indicating an increased probability of microtubule shrinkage events in the proximity of a glass surface. This finding is consistent with our observation of a reduction of microtubule shrinkage by a factor of 12 in the 3D system and agrees well with the fact that our 3D data analysis relies solely on microtubules that are at least 50 μm distant from any external boundary. Catastrophe events that are triggered by surface contact can be safely ruled out in the 3D analysis. This effectively allows for an unbiased quantification of the intrinsic contribution of microtubule shrinkage to microtubule dynamics. Additionally, the surface-to-volume ratio in the Teflon-based cylinders[11] over that in the conventional system is smaller by a factor of 50, reducing the depletion of proteins from the extract as a result of unspecific adsorption to the chamber's surface.

The 3D assay allowed us to measure a detailed microtubule growth speed distribution. We explicitly took growth speed changes within growth phases in single microtubules into account. We weighted the arithmetic speed distribution with the phase observation times (**Table 1**) and fitted a Gaussian distribution to the data within the detection window of growth speeds (data not shown), which corrects for the finite spatiotemporal resolution of the microscope. The Gaussian had a center at 9.71 ± 0.35 μm/min (s.e.m.; $n = 140$) and an s.d. of 2.94 μm/min, whereas the constrained 2D system provided the values 19.94 ± 0.29 μm/min (s.e.m.; $n = 172$) and 2.71 μm/min (**Fig. 3a**). The 3D assay s.d.

Table 1 | Comparison of 2D and 3D microtubule dynamic instability in interphase *X. laevis* egg extracts

Imaging	Sample preparation	Average v_g (μm/min)	S.d. of v_g (μm/min)	Average v_s (μm/min)	S.d. of v_s (μm/min)	Percentage growth	Percentage shrinkage	Percentage pause
2D	Slide- or coverslip-constrained	18.9 ± 0.3 ($n = 172$)	4.5 ($n = 172$)	12.1 ± 0.8 ($n = 70$)	6.9 ($n = 70$)	66.0	26.9	7.1
3D	Teflon cylinders, unconstrained	10.9 ± 0.6 ($n = 140$)	6.5 ($n = 140$)	12.8 ± 1.9 ($n = 20$)	8.3 ($n = 20$)	77.7	2.1	20.3

In total, we analyzed 16,488 s of microtubule dynamic instability in 156 microtubules. To obtain the average speeds and s.d., we weighted the arithmetic speed distributions with the phase observation times. The most prominent difference between the two systems is the probability of microtubule shrinkage. All indicated errors are errors of average values (s.e.m.).
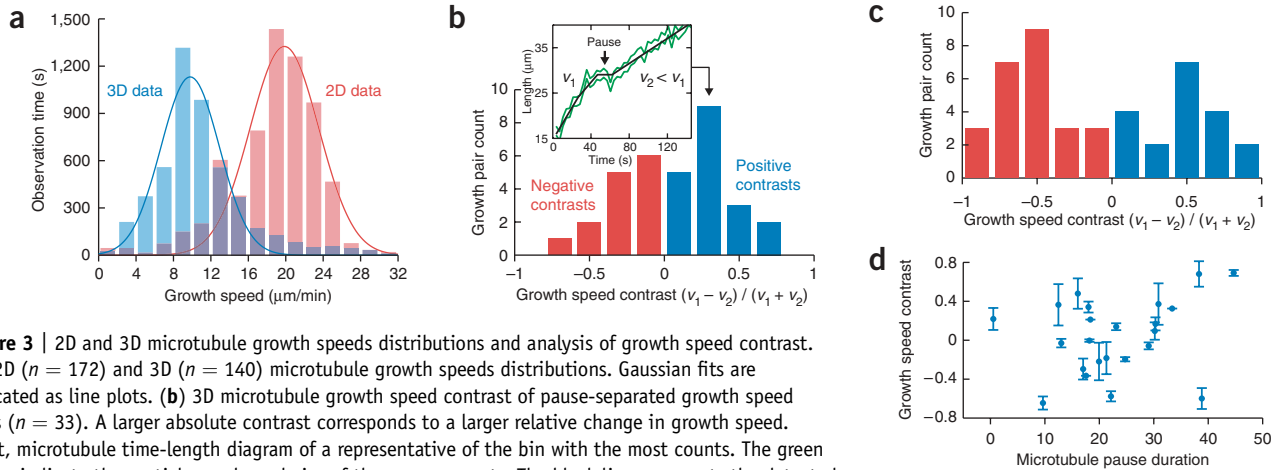
Figure 3 | 2D and 3D microtubule growth speeds distributions and analysis of growth speed contrast. (**a**) 2D ($n = 172$) and 3D ($n = 140$) microtubule growth speeds distributions. Gaussian fits are indicated as line plots. (**b**) 3D microtubule growth speed contrast of pause-separated growth speed pairs ($n = 33$). A larger absolute contrast corresponds to a larger relative change in growth speed. Inset, microtubule time-length diagram of a representative of the bin with the most counts. The green curves indicate the spatial error boundaries of the measurements. The black line represents the detected phases of the automated processing routines. (**c**) 3D microtubule growth speed contrast distribution of growth speed phases that are not separated by intermediate pauses or shrinkage phases ($n = 44$). (**d**) Analysis of the correlation between pause duration and growth speed contrast for data points for which both the contrast and the pause duration could be determined ($n = 23$). $R = 0.26$ (Pearson correlation). Error bars indicate the s.d. of fitted slopes.

reflects the intrinsic variability of microtubule growth speeds[12] and is related to molecular mechanisms that cause different growth speeds.

About 50% of the microtubules showed a switching of growth speeds during a growth speed phase or multiple growth phases separated by pauses. In all cases of multiple growth phases or speed switching, the speed changed by more than 10%. A 'growth speed contrast', c, which is defined as the difference between the two speeds divided by their sum, quantifies this phenomenon. We analyzed the growth contrast of 44 contiguous and of 33 growth phase pairs separated by a pause (**Fig. 3b,c**). Greater than twofold speed changes occurred for 36% of the contiguous growth pairs but only for 17% of the pause-separated growth pairs. In pause-separated pairs, the average contrast resulted in

$c = -0.27 \pm 0.06$ (s.e.m.; $n = 14$) for the situation of an increase and in $c = 0.33 \pm 0.04$ (s.e.m.; $n = 19$) for a decrease. For contiguous growth pairs, the average contrast resulted in $c = -0.54 \pm 0.04$ (s.e.m.; $n = 25$), for the situation of an increase and in $c = 0.46 \pm 0.05$ (s.e.m.; $n = 19$) for a decrease.

On average, changes within growth phases were a factor of two larger than those after intermediate pauses. In pause-separated phases, the duration of intermediate pause phases was not correlated to changes in growth speeds (**Fig. 3d**). As the main effects on microtubule growth speeds seem to originate from the presence of microtubule-associated proteins[13,14] and structural rearrangements (for example, a change in the protofilament number[15]), the occurrence of multiple growth changes in single microtubules and the symmetrical probability distribution of these

Figure 4 | T population statistics and its application in the analysis of microtubule pausing. (**a**) Determination of a global time frame for independent experiments by analyzing microtubule length distributions: microtubule length distributions of the entire asters were measured for the first 10 timepoints in all experiments (right). Linear regression of the average microtubule length yields the microtubule population growth speed J (middle) and the start time of microtubule polymerization (left). Error bars indicate s.e.m. (**b**) Distribution of microtubule pause durations ($n = 67$; including only those pauses, for which the start and end time points were recorded). (**c**) Frequencies of microtubule lengths in the pause state, derived by weighting the length counts at pause with the inverse global microtubule length distribution ($n = 86$). Error bars indicate s.e.m. (**d**) Correlation of microtubule pause duration and microtubule length in the length regime 10–35 µm ($n = 39$). (**e**) Correlation of microtubule pause duration and microtubule pause start time, derived by microtubule population statistics ($n = 48$). (**f**) Correlation of microtubule length and microtubule pause start time, derived by microtubule population statistics ($n = 39$). The red dashed line is a visual aid to highlight the positive correlation. Length error equals 0.99 µm. Pause duration error equals the sum of the temporal discretization error for start and end time points (3.67 s). Pause start error equals the sum of the global temporal axis error (3.35 s) and the discretisation error for the start time points (1.84 s).
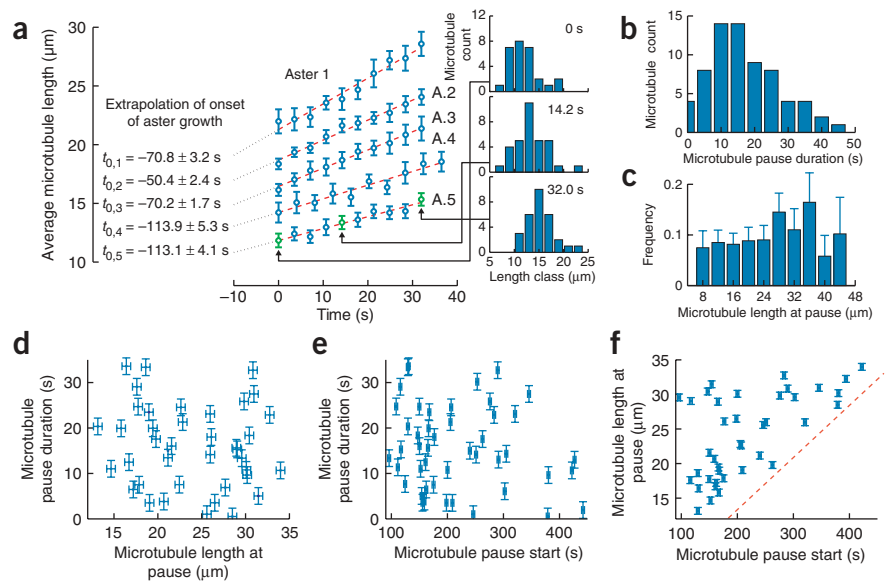
changes (centered at $c = 0$) indicate a potential reversibility of the underlying modifications.

Although many microtubules rapidly grow out of the focal plane in the 2D setup, 3D light-sheet based fluorescence imaging in combination with a 3D sample preparation facilitates time-resolved length measurements of all of an aster's filaments. Thus, the population growth speed, J, in dynamic equilibrium can be directly obtained from single asters. This allows for the computation of the onset of microtubule polymerization, and thereby, the combination of data from independently performed experiments (**Fig. 4a**). Phenomena otherwise not accessible owing to insufficient statistics become analyzable quantitatively. We used the assay to test the null hypothesis of a stochastic character of microtubule pausing events.

The asters showed a linear growth, as expected in a dynamic equilibrium (**Fig. 4a**). The average value resulted as $J_{average} = 9.1 \pm 1.2$ µm/min (s.e.m.; $n = 5$). We obtained the start time points of microtubule aster growth with a precision of $t_\Delta = 3.3 \pm 0.6$ s (s.e.m.; $n = 5$) and reconstructed the global time axis for five data sets.

We evaluated the distribution of microtubule pause durations (**Fig. 4b**). The arithmetic center of the distribution was 16.9 ± 1.3 s (s.e.m.; $n = 67$), the s.d. was 10.3 ± 1.3 s. An assessment of the microtubule lengths during pause phases showed that microtubule pausing is uncorrelated to the microtubules' length in the observed length regime 8–44 µm (**Fig. 4c**).

We used the global time axis to assess the time between the onset of microtubule aster polymerization and the occurrence of microtubule pause phases. We obtained an 87% confidence level for a zero-correlation between the microtubule lengths and the duration of the pause phases (**Fig. 4d**; Pearson correlation, $R = -0.027$) and a 78% confidence level for a zero-correlation between microtubule pause starts and pause phase durations (**Fig. 4e**, Pearson correlation, $R = -0.042$). The control measurement yielded a >99% confidence level for a nonzero-correlation of microtubule pause starts and microtubule lengths (**Fig. 4f**; Pearson correlation, $R = 0.586$), in agreement with the dynamic equilibrium condition.

Thus, neither the microtubule length nor the start timepoint of pausing are correlated to the pause phase's duration, and pausing can be regarded as a stochastic phenomenon. This experimental proof of a stochastic process is essential to support kinetic models of microtubule dynamic instability that characterize kinetic state transitions via average transition frequencies.

We developed a system for 3D measurements of microtubule dynamic instability that allow analysis of their intrinsic dynamic properties with a high spatiotemporal resolution and over long periods of time. Our quantification of microtubule dynamics in 3D reveals a strong dominance of microtubule pause over microtubule shrinkage in 3D and hence underlines the importance of the 'third state' of microtubule dynamic instability. These results reflect the need for the development of a comprehensive mathematical model of microtubule dynamic instability and suggest an investigation of the molecular mechanisms of microtubule pausing and its possible function in cells. Moreover, the measurements give direct access to 3D thermal fluctuations of the microtubules' shape and thus allow for an assessment of the microtubules' elastic properties in an unconstrained 3D system. It is particularly intriguing to perform these experiments in the physiological environment provided by the egg extract system.

Note: Supplementary information is available on the Nature Methods website.

AUTHOR CONTRIBUTIONS
P.J.K. developed the sample preparation in Teflon-based cylinders, performed the experiments, developed the image processing and data analysis algorithms and wrote most of the paper. F.P. trained P.J.K. in the biochemical aspects of the experiments and participated in project planning, in the 2D experiments and in manuscript preparation. E.H.K.S. outlined and supervised the project and participated in all stages of manuscript preparation.

1. Bray, D. *Cell Movements: From Molecules to Motility*. (Garland Publishing, New York, 2001).
2. Mitchison, T. & Kirschner, M. *Nature* **312**, 237–242 (1984).
3. Niethammer, P. *et al. PLoS Biol.* **5**, e29 (2007).
4. Waterman-Storer, C.M. *Mol. Biol. Cell* **9**, 3263–3271 (1998).
5. Grego, S., Cantillana, V. & Salmon, E.D. *Biophys. J.* **81**, 66–79 (2001).
6. Trinczek, B., Marx, A., Mandelkow, E.M., Murphy, D.B. & Mandelkow, E. *Mol. Biol. Cell* **4**, 323–335 (1993).
7. Dogterom, M. & Yurke, B. *Science* **278**, 856–860 (1997).
8. Yang, Y. *et al. J. Nanosci. Nanotechnol.* 2050–2056 (2005).
9. Janulevicius, A., van Pelt, J. & van Ooyen, A. *Biophys. J.* **90**, 788–798 (2006).
10. Huisken, J., Swoger, J., Del Bene, F., Wittbrodt, J. & Stelzer, E.H.K. *Science* **305**, 1007–1009 (2004).
11. Keller, P.J., Pampaloni, F. & Stelzer, E.H.K. *Curr. Opin. Cell Biol.* **18**, 117–124 (2006).
12. Pedigo, S. & Williams, R.C. Jr. *Biophys. J.* **83**, 1809–1819 (2002).
13. Arnal, I., Karsenti, E. & Hyman, A.A. *J. Cell Biol.* **149**, 767–774 (2000).
14. Shirasu-Hiza, M., Coughlin, P. & Mitchison, T. *J. Cell Biol.* **161**, 349–358 (2003).
15. Chrétien, D. & Fuller, S.D. *J. Mol. Biol.* **298**, 663–676 (2000).